Addressing Amorphization and Transgranular Fracture of B_4C through Si Doping and TiB_2 Microparticle Reinforcing

Chawon Hwang[1], Jun Du[1], Qirong Yang[1,†], Azmi M. Celik[1, ††], Kent Christian[1], Qi An[2], Mark C. Schaefer[1, †††], Kelvin Y. Xie[3], Jerry C. LaSalvia[4], Kevin J. Hemker[5], William A. Goddard III[6], Richard A. Haber[1,*]

[1] *Department of Materials Science and Engineering, Rutgers, The State University of New Jersey, Piscataway, NJ 08854, USA*

[2]*Department of Chemical and Materials Engineering, University of Nevada, Reno, Reno, Nevada 89577, USA*

[3]*Department of Materials Science and Engineering, Texas A&M University, College Station, TX 77843, USA*

[4]*DEVCOM Army Research Laboratory, Aberdeen Proving Ground, MD 21005, USA*

[5] *Department of Mechanical Engineering, Johns Hopkins University, Baltimore, MD 21218, USA*

[6]*Materials and Process Simulation Center, California Institute of Technology, Pasadena, California 91125, USA*

*Corresponding author e-mail: rich.haber@rutgers.edu, chawon.hwang@rutgers.edu, and address: 607 Taylor Road, Piscataway, NJ 08854, USA. Tel: +1 (848) 445-5924, FAX: +1 (732) 445-5926

This article has been accepted for publication and undergone full peer review but has not been through the copyediting, typesetting, pagination and proofreading process, which may lead to differences between this version and the Version of Record. Please cite this article as doi: 10.1111/jace.18223.

† Author's present address: *Materials Science Division, Lawrence Livermore National Laboratory, Livermore, CA 94550, USA*

†† Author's present address: *Department of Metallurgical and Materials Engineering, Gaziantep University, Gaziantep 27310, Turkey*

††† Author's present address: *Free Form Fibers, Saratoga Springs, NY 12866, USA*

Abstract

Over the last two decades, many studies have contributed to improving our understanding of the brittle failure mechanisms of boron carbide and provided a road map for inhibiting the underlying mechanisms and improving the mechanical response of boron carbide. This paper provides a review of the design and processing approaches utilized to address the amorphization and transgranular fracture of boron carbide, which are mainly based on what we have found through 9 years of work in the field of boron carbides as armor ceramics.

Keywords: Boron carbide; Doping; Titanium boride; Reinforcement; Amorphization; Fracture behavior

Introduction

With the pursuit of advanced lightweight protection materials that not only ensure the protection but also less hinders the mobility of personnel and vehicle, there has been an ever-

increasing demand for harder, lighter, and tougher armor ceramics.(1) In meeting the demand, boron carbide possesses the most potential because it is the hardest and lightest among the structural and impact-resistant ceramics for armor applications (Fig. 1).(2) Besides the extraordinary hardness and low density, it also displays high compressive strength and high melting point (~2350°C), which make boron carbide attractive for diverse applications under extreme environments, such as grinding materials and shielding components in nuclear reactors.(3, 4)

These remarkable properties of boron carbide are rooted in its strong covalent bonding between B (boron) and C (carbon) atoms, arranged into an icosahedron incorporated into a rhombohedral crystal structure (Fig. 2). While the exact crystal chemistry of boron carbide has been a subject of debate, most agree that the structure consists of two basic units, 12-atom icosahedra located at the vertices of the rhombohedral symmetry and a 3-atom chain connecting the icosahedra along the longest body diagonal.(11, 12) The low specific gravity of boron carbide can be attributed to a combination of light elements that constitute the compound and the icosahedral geometry that makes the crystal less dense. Extraordinary structural stability, strength, and hardness have also been documented in other covalent materials with near-spherical polyhedron configurations including fullerene molecules (13) and other icosahedra-based structures such as B_6O and α-boron.(14, 15)

Although the exceptional properties of boron carbide can be attributed to its unique crystal bonding and structure, it is also responsible for its limitations. As with other covalently bonded ceramics, boron carbide suffers from low lattice relaxation resulting in a limited modality of failure mechanism. The low packing density and low crystal symmetry imply that few slip systems are possible. Dislocation movement has not been observed in boron carbide subjected to deformation at ambient temperature (except for amorphization mediated dislocation).(16, 17) Expectantly, the

predominant failure mode of boron carbide is brittle fracture, and the fracture mode is transgranular, shown in Fig. 3A.(18-20) Under high-pressure loading scenarios, such as indentation, diamond anvil compression, laser shock, and ballistic impact, boron carbide also fails through a competing mechanism known as stress-induced amorphization (Fig. 3B).(21-25) This stress-induced deformation mechanism has been described as an inhomogeneous loss of crystalline order in localized zones scattered within a crystalline volume, forming nanoscale bands with large aspect ratios (i.e. nanoscale shear bands). Such amorphous bands act as a "path of least resistance" for crack nucleation and propagation, leading to an accelerated fragmentation and an abrupt loss of shear strength. The two dominant failure modes, transgranular fracture and amorphization, limit employing boron carbide as materials for structural applications, especially as armor ceramics against high-speed projectiles.

The transgranular fracture mode of boron carbide is a consequence of strong grain boundary cohesive strength.(25) One possible way to alter the fracture behavior of boron carbide is to form a microstructural-level composite with a secondary phase reinforcement. The reinforcement of transition-metal diborides has shown to hinder the propagation of crack and alter its traveling mode in boron carbide.(27, 28) On the other hand, atomic doping has demonstrated to be a viable method to suppress amorphization.(23, 29-31) Therefore, a solution comprised of microstructural reinforcement and atomic doping could address both failure mechanisms of boron carbide simultaneously.

This paper summarizes 9 years of work in the field of boron carbides and discusses a multiscale design and processing strategy that encompasses atomic-level doping and microstructural-level reinforcement to address the two major failure modes of boron carbide chosen by the authors: Amorphization and transgranular fracture. This paper is divided into three sections: 1) Improving the tolerance of boron carbide to amorphization via atomic doping, 2) Altering the fracture behavior of

boron carbide through microparticle reinforcement, and 3) Addressing both failure modes of boron carbide simultaneously by combining atomic doping and microparticle reinforcement. In addition, we also identified opportunities that have the potential to further enhance the multiscale design and processing strategy.

Part 1. Atomic doping to improve the tolerance of boron carbide to amorphization

Observation of amorphization in boron carbide (B_4C)

The phenomenon of amorphization in boron carbide was first discovered through a Raman study on an indented boron carbide by Domnich et al.(21). A boron carbide single crystal ($B_{4.3}C$) was indented at a small load (100 mN) and the change in Raman spectrum before and after indentation was observed (Fig. 4a and b). The most dramatic changes after indentation were the appearance of new Raman bands between 1200-2000 cm^{-1}, the most intense of which is at ~ 1330 cm^{-1} (Fig. 4b). Considering that the peak at ~ 1330 cm^{-1} is close to the D band of amorphous (glassy) carbon, it is surmised that the high-pressure contact loading (~40 GPa) during indentation may have caused a stress-induced phase transformation to a disordered structure, i.e. amorphization, in boron carbide.

TEM observations of post-impacted boron carbide fragments by Chen et al. (25) directly revealed and confirmed the presence of amorphous boron carbide (Fig 3b). The observed amorphous bands were found to be several nanometers across and hundreds of nanometers in length. Chen's TEM study involved ballistic-impacted boron carbide fragments that were impacted above and below the critical impact velocity for comminution (~ 850 m/s). The nanoscale amorphous bands were observed in fragments that were impacted at velocities above the critical velocity but not for those

below it.(25) At the higher velocities, the impact pressure is sufficiently large, surpassing the Hugoniot elastic limit (HEL) of boron carbide (20 GPa), to cause irreversible deformation and fast fracture.(32, 33) The long and narrow geometry of the amorphous bands was first associated with catastrophic collapse and highly localized softening of the boron carbide lattice. However, long thin amorphous bands have since been observed and associated with a wide variety of loading conditions (ballistic impact(25), indentation(21), scratching(34), etc.(22, 24)), and shear loading is now widely accepted to be a requisite condition for amorphization. Later the atomic structure of amorphous bands has been further revealed by Reddy et al.(35) that the amorphous shear bands preferentially take place along the particular crystal plane $(01\bar{1}\bar{1})$ that is comprised of aligned three-atom chains (Fig. 5).

Theoretical studies on the mechanism of amorphization in boron carbide

The experimental observation of the stress-induced amorphization in boron carbide motivated numerous theoretical studies aimed at understanding the mechanism of amorphization in boron carbide.(22, 36-39)

Density functional theory (DFT) simulations have been used to investigate the initial bond deformation, bond breaking, and formation, as well as the icosahedra deconstruction during amorphization.(22, 36, 38)

An et al. examined the shear-induced structure failure of B_4C along 11 plausible slip systems using DFT simulations.(38) They found that, among the 11 slips systems, the shear along $(01\bar{1}\bar{1})/[\bar{1}101]$ slip system has the lowest ideal shear strength of ~40 GPa, is much lower than the compression/tension strength from other DFT work.(22, 36, 37)

This finding provides the foundation that shear plays an important role in the mechanical failure of B_4C and its amorphization. The DFT-derived deformation mechanism along this slip system is illustrated in Fig. 6. Firstly, shear breaks the inter-icosahedral B-C bonds as the icosahedral layers slipped relative to each other (Fig. 6b). This leads to the formation of carbene with one lone pair, making it very reactive to positively charged atoms. Then the C-B-C chain approaches the carbene with further shear deformation (Fig. 6c), leading to the Lewis acidic B in the chain to bond with the carbene, which results in the irreversible deconstruction of the icosahedra (Fig. 6d), i.e. shear stress-induced amorphization.

These DFT studies involve cells too small to observe amorphous shear bands so Qi and Goddard used ReaxFF reactive dynamics simulations to observe the shear induced deformation of a ~20 nm by 20 nm single crystal, where they observed first twinning, then formation of a 2~3 nm shear band that later underwent cavitation and crack formation.(39) They found that breaking the icosahedron increased the density leading to tension that caused the cavitation and failure.

A theoretical suggestion of amorphization mitigation via atomic doping

The modeling and simulation studies on the mechanism of stress-induced amorphization in B_4C suggested that it is important to prevent the interaction between the chain and cage to avoid the deconstruction of the icosahedral clusters. Furthermore, this suggested that substituting the C-B-C chain with a two-atom chain might completely suppress the deconstruction of icosahedra, leading to a mitigated amorphization in B_4C.(40, 41) One promising element to form a two-atom chain is silicon, Si.(40) The DFT simulations on the $(B_{11}C_p)Si_2$ system showed that the icosahedra are not

deconstructed under shear deformation, as shown in Fig. 7.(40) Instead, the three bonds of each Si to the icosahedra break one bond but keeping the other two as it migrates to form the 3rd bond to neighboring icosahedra. Thus, the icosahedra remain stable during this shearing. This study provided the theoretical logic for doping boron carbide with Si to mitigate its amorphization.

Experimental preparation of monolithic doped boron carbides

Available methods to dope boron carbide with elements

The theoretical suggestion doping boron carbide with Si encouraged studies to prepare Si/B co-doped boron carbide ceramics. To dope boron carbide with Si and B, a variety of methods have been utilized. These methods include pressureless sintering, reaction bonding, high-energy ball milling, arc melting, nanorod growth, and pressure-assisted sintering.(23) The different methods entail boron carbides with different characteristics, such as different degrees of densification and doping as well as the presence of a secondary or residual phase. Preferred methods should minimize the formation of undesirable secondary or residual phase while ensuring full densification, high content of doping elements, and scalability.(19, 42)

Pressureless sintering methods have an advantage in producing boron carbide with complex shape without the need for extensive post machining.(43) Despite the advantage, it alone is not suitable for reaching full densification of boron carbide.(44) Sintering additives have been utilized to improve densification, but they typically lead to the formation of undesirable secondary phase, which negatively impacts the mechanical properties of boron carbide.(45, 46)

Reaction bonding can be used to produce Si/B co-doped boron carbide by infiltrating porous boron carbide with a molten silicon source, which then reacts with boron carbide to form a doped phase.(47, 48) However, the presence of residual un-reacted Si is inevitable, which has poor mechanical properties and thermal stability compared to boron carbide.(48) Powder shape of Si/B co-doped boron carbide also can be synthesized through high-energy ball milling and arc melting.(23, 49-51) High-energy ball milling possesses the merit of operating at low temperature (<500 °C), which allows for doping boron carbide while suppressing the formation of the undesirable secondary phase. Whereas, arc melting process utilizes high temperature (>3,000 °C) that allows for higher contents of doping elements. However, the feasibility of utilizing the doped boron carbide powders synthesized through the high-energy ball milling and arc melting process has not been established yet to produce doped boron carbide bulk ceramics. Growing nanorods of Si-doped boron carbide through a solid-liquid-solid process has also been explored.(52) Though the process achieved doping content of Si between 0.6-1.6 at%, it is not suitable for producing large-size bulks due to the low production yield of the process.

Up to date, pressure-assisted reactive sintering processes can be regarded as the most efficient route to produce dense Si/B co-doped boron carbides. By applying pressure, higher density can be obtained at lower temperatures compared to pressureless sintering, and by reacting boron carbide with doping sources, doping can be achieved.(53, 54) The two most common pressure-assisted sintering techniques are hot press sintering (HP) and spark plasma sintering (SPS).

Preparation of Si/B co-doped boron carbides through a pressure-assisted reactive sintering process

Dense (99.6% TD) large tiles (120 x 120 x 1.3 cm) of Si/B co-doped boron carbide were prepared by reactive hot pressing a particulate mixture of B_4C (a base powder), SiB_6 (a source of Si and B), amorphous B (a source of B).(28) SiB_6 is chosen over Si for its higher melting point (1950°C vs 1414°C of Si), which allows for pressure to be applied at higher temperatures. The additional B is to adjust the B/C ratio to roughly 6.5, where the solubility of Si is the highest.(44) The reaction hot-pressing is carried out at 1950°C for 3 hours at 20 MPa.

The chemistry of the as-sintered Si/B co-doped boron carbide was characterized using XRD and Raman spectroscopy (Fig. 8) and compared to a commercially available undoped B_4C tile (PAD B_4C; CoorsTek). Using XRD, only the boron carbide phase was identified in the Si/B co-doped boron carbide, whereas C and BN were identified in the PAD B_4C in addition to the boron carbide phase. The enlarged section shows a downshifting in the (021) peak reflection, which indicates that the Si/B co-doped boron carbide has a larger unit cell.(53) Raman spectra also show the salient differences between the doped and undoped boron carbide. Compared to the PAD B_4C, the spectrum of Si/B co-doped boron carbide shows two Si-doping peaks at 240 and 1120 cm^{-1} peaks.(23, 28, 53) And the decrease in the 478 cm^{-1} peak intensity relative to the 530 cm^{-1} peak suggests that the strong C-B-C chains are replaced by weaker C-Si-C chains. Lastly, a downshift in the 1190 cm^{-1} peak suggests that the Si/B co-doped boron carbide has larger icosahedra compared to the undoped PAD B_4C.

The microstructure of the as-sintered Si/B co-doped boron carbide has an average grain size of 79.8 ± 11.0 μm, compared to 11.2 ± 1.5 μm of the PAD B_4C. A secondary phase rich in Si and O was found throughout the microstructure of the Si/B co-doped boron carbide. The lack of X-ray diffraction peaks suggests that the secondary phase is likely amorphous SiO_2 introduced by the SiB_6 powders as a surface oxide. During the sintering process, transient liquids with various compositions

form through the eutectic reactions in the B-C-Si system and the melting of SiB_6.(44) And the presence of liquid phases lowers the sintering conditions for boron carbide, requiring only 1950 °C at 20 MPa to achieve >99% TD, as compared to >2100 °C at 30-40 MPa to achieve >95% TD for liquid phase-free sintering.(51, 55, 56) It accelerated the kinetics of sintering, but also resulted in exaggerated grain growth as seen in Fig. 8c.

Effect of Si/B co-doping on amorphization and properties of boron carbides

Raman analysis was carried out to assess the effect of Si/B co-doping on amorphization. The amorphization intensity inside of residual imprints is illustrated as color maps in Fig. 9a. The amorphization is contained entirely inside of the residual imprint and the highest intensity is located near the center where it experienced the highest pressure during indentation. By normalizing the amorphized area by the indentation size, we found 41 and 27% of the impression is amorphized in the PAD B_4C and Si/B co-doped boron carbide, respectively, which equates to a reduction of 34% of amorphous area reduction. The histogram of the pixels is illustrated in Fig. 9b to further understand the extent of reduction. Si/B co-doping is most effective at suppressing the higher intensity pixels (marked by arrows), which is presented by smaller high intensity near the center of the impression in Fig. 9a. By integrating the pixel intensity, we obtained a reduction of 44% in the total amorphous intensity in the Si/B co-doped boron carbide. It should be noted that the above evaluation of amorphization is based on a quasi-static indentation of boron carbide, which is different from a dynamic indentation where the imprint is created for a short time frame, on the order of 60 - 100 μs. The effect of stress state and strain rate on the amorphization of un-doped boron carbides can be found in the literature.(57, 58)

The mechanical and physical properties of the Si/B co-doped boron carbide and PAD B_4C are summarized in Table 1. There is an overall reduction in mechanical properties due to Si/B co-doping, notably a decrease in Vickers hardness (-5%), indentation fracture toughness (-13%), and flexural strength (-15%). Interestingly, Si/B co-doped boron carbide shows an improvement in the Young's modulus by 6%. The density of both samples is roughly the same. The reduction in the mechanical properties can be partially attributed to microstructural effects, such as residual porosity, the presence of SiO_2, and the increase in the grain size, which has shown to negatively impact the mechanical properties due to the Hall-Petch relationship.(59) The presence of Si- and/or B-containing melt during reactive sintering facilitated the exaggerated grain growth. As a result, the grain size of Si/B co-doped boron carbide is six times greater than that of the PAD B_4C. The reduction in mechanical properties can also be explained by the changes in atomic bonding strength. Si/B co-doping lengthens the bonds in the crystal structure of boron carbide, evident by the peak shifting in the XRD pattern and Raman spectrum in Fig. 8. In covalently bonded solids, longer bonds are weaker, thus reduced mechanical properties can be anticipated. Furthermore, doping also replaces the stronger C-B-C bonds with C-Si-C bonds as pointed out in the previous section. Taken together, the Si/B co-doped boron carbide shows a reduction in amorphization but also a reduction in mechanical properties.

Part 2. Microparticle reinforcement to alter the fracture behavior of boron carbide

Fracture behavior of boron carbide and an improvement strategy

Like most ceramics, strong covalent bonds confer boron carbide high hardness and high stiffness, but also brittle fracture.(11, 55) For example, Chen et al. observed that boron carbide experiences brittle fracture during impact tests, showing typical cleavage surface in fragments (Fig.

10).(25) In addition, the intrinsically strong grain boundaries of polycrystalline boron carbide permit crack propagation only in a transgranular manner.(20, 60) Taken together, boron carbide has a low toughness, ~2.5 $MPa \cdot m^{1/2}$ (indentation fracture toughness), which limits its use for structural applications.

Toughening strategies have been developed to address the two aspects accordingly. First, altering bonding nature through atomic doping is conceivable, but how to realize this in reality is extremely challenging. Moreover, studies on boron carbide doped with boron or silicon showed an adverse effect of doping on the indentation fracture toughness of boron carbide, as pointed out in the previous sections.(28, 61) Therefore, more attempts were focused on toughening boron carbide by modifying its fracture behavior. Adding a "tougher" reinforcement to activate additional toughening mechanisms is a proven strategy. Transition metal borides and carbides are of particular interest because of their excellent compatibility with the boron carbide matrix. More importantly, they are tougher than boron carbide while being similarly hard. Table 2 summarizes the representative boron carbide composites, such as B_4C-SiC, B_4C-TiB_2, and B_4C-ZrB_2, along with the processing methods, sintering conditions, and properties. The toughness and hardness change relative to boron carbide (B_4C) monolith is shown in Figure 11. In contrast to boron carbide, significant improvement (~60%-100%) in the toughness has been achieved by adding reinforcement of SiC, TiB_2, and ZrB_2. A drop in hardness, about 10-20%, was observed, since boron carbide is harder than any of the reinforcement phases. Here, we focused more on TiB_2 reinforcement for two reasons. First, it provides a high toughness improvement with a comparatively less hardness reduction. Moreover, it has the lowest density in the group of transition metal borides, which is of benefit in suppressing the density penalty accompanied by the addition of heavy reinforcement. It should be noted that the following sections

are mainly focusing on the authors' work. For more comprehensive understanding of the approach, the readers are recommended to refer to other important work, such as the study on the topic of deformation and failure mechanisms under quasi-static and dynamic loading in B_4C-TiB_2 composites.(26)

Preparation and characterization of TiB_2 reinforced boron carbides

There have been numerous attempts to incorporate TiB_2 as a reinforcement phase into B_4C ceramics.(66, 67, 70-72) B_4C-TiB_2 composites had been prepared by pressure-assisted sintering particulate mixtures of B_4C and TiB_2.(66, 67) Reactive sintering had also been utilized to sinter B_4C-TiB_2 composites by using reactions between B_4C, TiO_2, and carbon. Fine-grained (<1 μm) B_4C-15 vol.% TiB_2 composite exhibited high Vickers hardness of 36.9 GPa and outstanding flexural strength of 724 MPa.(72) Sigl et al. consolidated B_4C-TiB_2 composites through pressureless sintering followed by HIP (hot isostatic pressing) at 2050 ºC and 200 MPa.(71) More recently, sputter deposition of TiB_2 on B_4C powders was utilized to hot press B_4C-TiB_2 composites with a small amount of well-dispersed TiB_2 particulates. Indentation fracture toughness of B_4C was improved by 15% with the addition of 2.3 wt.% TiB_2, while its bulk density was only 2% higher than that of a monolithic B_4C.(27)

To reinforce B_4C with TiB_2, commercial powders of B_4C (Grade HD20, H.C. Starck, d_{50}=0.7 μm) and TiB_2 (Grade F, H.C. Starck, d_{50}=2.5 μm) were used.(73) Since TiB_2, (4.52 g/cm^3) has a higher density than boron carbide (2.52 g/cm^3), only small amount of TiB_2 (up to 15 wt%) was considered to minimize the increase in density, which is one of the critical factors for armor

applications. Dense (>99% TD) B_4C-TiB_2 disks (> 100 mm diameter) were successfully fabricated at 2150ºC and 24 MPa for 2 hours in Ar gas.

X-ray diffraction pattern of B_4C-10% TiB_2 composite as-sintered is shown in Fig. 12 along with those of starting powders. Primary peaks obtained in the composite belong to the B_4C and TiB_2 phases. No other peaks were identified, except for a minor graphitic peak at ~26.5°, which is indicative of a small amount of free carbon pre-existing in the starting boron carbide.

Fig. 13 shows the microstructures of the B_4C reinforced with 10% TiB_2. The secondary electron images (Fig. 13a & b) confirm that the composite is dense. Phase contrast is from the difference in atomic number (Z), i.e., the bright phase contains higher Z elements, Ti in this case. TiB_2 particles have an average size of 1.3 μm and were uniformly distributed throughout the material (see Fig. 13a & b). The spatial distribution of reinforcement can be critical to the reliability of material. The grain size of the matrix phase, B_4C, was measured to be 1.6 μm (see Fig. 13c). In general, the processing of boron carbide requires high temperatures (close to its melting point) and long dwelling times for full densification, leading to the formation of large grains. For example, boron carbide processed at identical conditions gives a grain size of ~17.0 μm (see Fig. 13d). However, the addition of TiB_2 could impede the grain boundary movement, resulting in refined grains. This finding is consistent with results in the literature.(26) The grain size and density are summarized in Table 3.

Mechanical properties of B_4C-10%TiB_2 composite, including hardness and indentation fracture toughness, are summarized in Table 4. In contrast to commercial armor-grade boron carbide (PAD B_4C), a notable increase (>20%) in hardness has been achieved. This can be attributed to the Hall-Petch relationship as a result of the grain size refinement by TiB_2 addition. In addition, commercial boron carbide often contains impurities like AlN and Fe-based alloys, which are

detrimental to hardness.(19, 20) For example, monolithic B_4C produced from high purity powders exhibits a higher hardness value, ~29 GPa. Reinforcing B_4C with TiB_2 also improved i) toughness by activating additional energy dissipation mechanisms upon a crack propagates, such as crack deflection and crack bridging, as well as ii) elastic modulus because of the high stiffness of the TiB_2 phase (E, 565 GPa).(74) Moreover, there is only a minor increase in the density of boron carbide composite.

The crack propagation behavior of TiB_2 reinforced B_4C was investigated in detail. The Vickers indentation method was used to initiate controlled damage to the composite, as shown in Fig 14a, where radial cracks emanated from corners of the pyramid. Most of the crack paths show a nonlinear profile across the specimen. Fig. 14b shows a closer observation of the crack path near the crack tip. As expected, the boron carbide matrix fractured in a transgranular manner.(20, 25, 60) However, the crack was deflected at the interface between the matrix (B_4C) and the reinforcement (TiB_2), as reported in the literature.(75, 76) This can be attributed to the residual stress built by the lattice and thermal mismatches between B_4C and TiB_2 phase.(12, 74, 77), which is estimated to be ~500 MPa(27, 78). Taken together, the B_4C-TiB_2 composite displays a mixture of transgranular and intergranular fracture modes.

Part 3. Combining atomic doping and microparticle reinforcement to prepare boron carbide with improved amorphization tolerance and fracture behavior

Preparation and characterization of Si/B co-doped TiB_2 reinforced boron carbides

As discussed in Part 1, atomic doping boron carbide with Si and B has proven to be an effective strategy for suppressing amorphization.(23, 29) However, the improved amorphization

resistance of boron carbide by atomic doping was achieved at the expense of degradation in hardness and toughness. This was attributed to weaker covalent bonds and exaggerated grain growth, both caused by doping.(79, 80) Since hardness weighs heavily in the ballistic performance of boron carbide, compensation of hardness loss should be considered for designing boron carbide as lightweight protection materials.(11, 81) An effective design strategy to overcome this issue is to reinforce doped boron carbide with a tough and hard reinforcement. As shown in Part 2, TiB_2 reinforced boron carbide displays high hardness, high toughness, and comparably low density. Thus, it is conceivable that a TiB_2 reinforced Si/B co-doped boron carbide could possess enhance amorphization resistance without compromising the mechanical properties.

Bulk Si/B co-doped boron carbide reinforce with TiB_2 (denoted as Si-BC/TiB_2) was prepared by reactive hot pressing particulate mixtures of B_4C, SiB_6, B, and TiB_2 at 1950 ºC and 20 MPa for 3 hours in Ar gas.(28) The chemistry of Si-BC/TiB_2 was designed to be nominally 1.5 at% Si-$B_{6.5}C$/10 wt% TiB_2. Large square tiles (107 x 107 x 13 mm) were successfully produced, having a density of 2.59 g/cm^3, which corresponds to 99.2% of the theoretical density (2.61 g/cm^3 from a rule of mixture).

Fig. 15 shows the microstructure of the Si-BC/TiB_2. Almost no sintering pores were seen in the microstructure (Fig. 15a and 15b), which validates the high relative density. The bright phase is TiB_2 reinforcement particles, uniformly distributed throughout the material. A closer observation of the matrix (Fig. 15b) identified a minor secondary phase (later confirmed the SiO_2-rich phase). Fine grain size of 1.5 μm was measured on average (Fig. 15c). In contrast, a grain size of ~80 μm was reported in silicon doped boron carbide processed at similar conditions, because a rapid grain growth occurred.(28) This discrepancy in grain size can be attributed to the addition of reinforcement particles, as TiB_2 does not diffuse easily and thus impedes grain boundary movement, refining grain

growth. Similar results were observed in other systems, like SiC/TiB_2(82) and B_4C/TiB_2(27). Occasionally, a few large grains in tens of microns were observed in the microstructure, which is possibly due to agglomerates in powder mixing.

X-ray patterns and Raman spectrum of Si-BC/TiB_2 are shown in Fig. 16, where B_4C/TiB_2 was also listed as a reference. The peaks obtained in Si-BC/TiB_2 belong to those of boron carbide and titanium diboride phases. A downshift in peak positions of Si-BC matrix, i.e., $(021)_{Si\text{-}BC}$, indicates a lattice expansion due to Si/B co-doping, which is also observed in Si/B co-doped boron carbide (Part 1). Little change was observed in the peak position of TiB_2 phase, since Si does not dissolve into the TiB_2 phase. Raman analysis (Fig. 16b) further points to the Si/B co-doping in boron carbide, evident by the formation of the 210/240 cm^{-1} doublet(23, 47, 53) and 1170 cm^{-1} peak(61, 80). In addition, the downshift in the 1090 cm^{-1} Raman band with respect to the B_4C matrix in B_4C/TiB_2 composite also indicates larger unit cells due to B-enrichment in the icosahedra. TiB_2 is not Raman active and gives no signals.

Amorphization mitigation, fracture behavior, and properties of Si/B co-doped TiB_2 reinforced boron carbides

Amorphization induced by the indentation method was semi-quantified by Raman spectroscopy. The average amorphization intensity inside of residual imprints is illustrated as pseudo color maps in Fig. 17.(28) The highest intensity was predominantly at the center of the imprint, where it experienced the highest pressure during indentation. By normalizing the amorphized area by the indentation size, we found 31% and 44% area was amorphized inside the imprint for Si-BC/TiB_2 and B_4C/TiB_2, respectively. In other words, those are reductions of 30% in amorphous areas from

B_4C/TiB_2 to Si-BC/TiB_2. Since each pixel carries an intensity, the summation of the intensities, after accounting for the indentation size, can also estimate the overall reduction in amorphization intensity. The cumulative sum of the amorphization intensity yields a reduction of up to 44% from B_4C/TiB_2 to Si-BC/TiB_2.

Fig. 18 illustrates how cracks propagate through Si-BC/TiB_2. The crack path is clearly nonlinear but deflected at phase boundary as a result of residual stress built at the interface.(27, 83) The termination of crack by a TiB_2 grain can also be found. Taken together, the addition of TiB_2 changed the crack propagation behavior of Si/B co-doped boron carbide from intergranular to a mixed mode of intergranular and transgranular, as shown in Fig. 18.

The mechanical and physical properties of the Si-BC/TiB_2 are summarized in Table 5. As mentioned earlier, silicon doped boron carbide (Si-BC) showed overall inferior mechanical properties as compared to undoped commercial boron carbide (B_4C), notably a substantial decrease in indentation fracture toughness (K_{Ic}, -13%) and flexural strength (σ_f, -15%). The reduction can be attributed to the weakening of atomic bonding strength, exaggerated grain growth, and formation of secondary phase inclusions as discussed in Part 1. However, the degradation in mechanical properties could be effectively compensated by the incorporation of TiB_2. For example, 10% TiB_2 addition witnessed the increases of 6% in Hv, 8% in K_{Ic}, and 18% in σ_f, when compared to Si-BC, making Si-BC/TiB_2 comparable to commercially available armor-grade B_4C (PAD B_4C). Moreover, there is only a minor increase in density, which can be attractive for armor applications. More importantly, Si-BC/TiB_2 preserved superior resistance to amorphization. Taken together, boron carbide with improved amorphization tolerance and fracture behavior was demonstrated by combining the approaches of atomic doping and microparticle reinforcement.

Opportunities

Throughout this paper, we identified two key opportunities to further improve the amorphization mitigation and fracture behavior of boron carbide.

Based on a number of studies(23, 53, 84), it is conceivable that increasing Si doping amount of boron carbide may further enhance its tolerance to amorphization. Altering the chemistry of boron carbide to a more boron-rich composition remains as the principal technique to increase the Si doping amount (i.e. Si solubility) in boron carbide.(23, 53) According to the phase equilibrium of B-C-Si, the solubility of Si in boron carbide maximizes near a B to C ratio of approximately 6.5.(44, 85) Further increases in the Si solubility are expected to afford even more amorphization resistance to boron carbides.(85) Toward this end, arc melting has been suggested as a processing route to synthesize pre-reacted powder of boron carbide with higher Si content than normally obtainable by reaction sintering.(23) This is because the solubility of Si at arc melting temperatures, typically >3000 °C(23, 86), is expected to be significantly higher than the solubility at sintering temperatures, typically 1600 ~ 2100 °C(60).(50) The approach of Si/B co-doping may be combined with arc melt processing to further increase the Si solubility and benefit from potentially enhanced amorphization mitigation.

Secondly, microparticle reinforcement using TiB_2 particulate has proven effective in toughening and altering the fracture behavior of boron carbide. A further improvement may be achievable by optimizing the morphology of TiB_2 reinforcement. The aspect ratio of reinforcement particles has been found critical in determining the toughness and fracture behavior of composites in various material systems, including polymers(87), cement(88), and ceramics(89). For example,

needlelike β-Si_3N_4 grains were found more efficient in promoting crack deflection (more new surface areas created to dissipate elastic energy), leading to a high toughness of more than 8 $MPa \cdot m^{1/2}$ (indentation fracture toughness). Similarly, a study showed that increasing the aspect ratio of TiB_2 reinforcement improves the toughness of the B_4C-TiB_2 composite.(90) In the previous section of reinforcing Si/B co-doped boron carbide (Part 3), commercially available TiB_2 powders with irregular morphology and low aspect ratio (closer to equiaxial particle) were used. Thus, it is suggested that the fracture behavior and toughness of Si/B co-doped boron carbide could be further enhanced by using TiB_2 reinforcement with higher aspect ratios, such as TiB_2 powder synthesized by a carbothermal reduction process or TiB_2 whisker/fiber/platelet, though the sintering may require enhanced conditions for full densification.

It is noteworthy that, besides the above approaches based on atomic doping and microparticle reinforcement, one can also consider other approaches to mitigate the amorphization tendency and improve the fracture behavior of boron carbide. Through a theoretical simulation as well as experimental observation on nanocrystalline boron carbide, prepared by high pressure high temperature processing (1 GPa and 1600°C), it was reported that reducing grain size to nanoscale promotes the plastic deformation of boron carbide, retarding amorphization to occur at higher shear stains, as well as the intergranular fracture of boron carbide rather than transgranular fracture.(91, 92) In addition, forming graphene or graphene oxide at grain boundaries proved to be effective in deflecting the propagation of the cracks in boron carbides.(93, 94)

Acknowledgments

This research was sponsored by and was accomplished under the Army Research Laboratory under Cooperative Agreement [W911NF-12-2-0022]. Additional support was received from Defense Advanced Research Projects Agency [Grant No.: W31P4Q-13-1-0001] and the National Science Foundation I/UCRC [Award No.: 1540027]. The authors acknowledge Vladislav Domnich of Ferro Corporation and Atta U. Khan of Collins Aerospace for their insightful discussion. This work was performed under the auspices of the U.S. Department of Energy by Lawrence Livermore National Laboratory under Contract DE-AC52-07NA27344.

References

1. Fish L, Scharre P. The Soldier's Heavy Load. Super Soldiers series: The Center for a New American Security 2018. p. 1-20.

2. Matchen B. Applications of Ceramics in Armor Products. Key Engineering Materials. 1996;122-124:333-44.

3. Paliwal B, Ramesh KT. Effect of crack growth dynamics on the rate-sensitive behavior of hot-pressed boron carbide. Scripta Materialia. 2007;57(6):481-4.

4. Suri AK, Subramanian C, Sonber JK, Murthy TSRC. Synthesis and consolidation of boron carbide: a review. International Materials Reviews. 2010;55(1):4-40.

5. Gao F, He J, Wu E, Liu S, Yu D, Li D, et al. Hardness of Covalent Crystals. Physical Review Letters. 2003;91(1).

6. Vassen, Robert, Stöver, Detlev. Processing and Properties of Nanograin Silicon Carbide. Journal of the American Ceramic Society. 1999;82(10):2585-93.

7. Shacklford JF, Alexander W. CRC Mater. Sci. & Eng. Handbook: CRC Press LLC; 2001.

8. Tsai K-M, Hsieh C-Y, Lu H-H. Sintering of binderless tungsten carbide. Ceramics International. 2010;36(2):689-92.

9. Bansal NP. Handbook of Ceramic Composite: Springer; 2005.

10. Moshtaghioun BM, Ortiz AL, Gómez-García D, Domínguez-Rodríguez A. Toughening of super-hard ultra-fine grained B_4C densified by spark-plasma sintering via SiC addition. Journal of the European Ceramic Society. 2013;33(8):1395-401.

11. Domnich V, Reynaud S, Haber RA, Manish C. Boron Carbide: Structure, Properties, and Stability under Stress. Journal of the American Ceramic Society. 2011;94(11):3605-28.

12. Aselage T, Tissot R. Lattice constants of boron carbides. Journal of the American Ceramic Society. 1992;75(8):2207-12.

13. Krätschmer W, Lamb L, Fostiropoulos K, Huffman D. Solid C_{60}: a new form of carbon. Nature. 1990;347(6291):354-8.

14. Hubert H, Devouard B, Garvie L, O'Keeffe M, Buseck P, Petuskey W. Icosahedral packing of B_{12} icosahedra in boron suboxide (B_6O). Nature. 1998;391(6665):376-8.

15. Parakhonskiy G, Vtech V, Dubrovinskaia N, Caracas R, Dubrovinsky L. Raman spectroscopy investigation of alpha boron at elevated pressures and temperatures. Solid State Communications. 2013;154:34-9.

16. Reddy KM, Guo D, Song S, Cheng C, Han J, Wang X, et al. Dislocation-mediated shear amorphization in boron carbide. Science Advances. 2021;7(8):eabc6714.

17. Subhash G, Awasthi A, Kunka C, Jannotti P, DeVries M. In search of amorphization-resistant boron carbide. Scripta Materialia. 2016;123:158-62.

18. Swab J, Pittari IJ, Gamble W. Uniaxial tensile strength and fracture analysis of a hot-pressed boron carbide. Journal of the European Ceramic Society. 2019;39(6):1965-73.

19. Chen M, McCauley J, LaSalvia J, Hemker K. Microstructural Characterization of Commercial Hot-Pressed Boron Carbide Ceramics. Journal of the American Ceramic Society. 2005;88(7):1935-42.

20. Xie KY, Kuwelkar K, Haber RA, LaSalvia JC, Hemker KJ. Microstructural Characterization of a Commercial Hot-Pressed Boron Carbide Armor Plate. Journal of the American Ceramic Society. 2016;99(8):2834-41.

21. Domnich V, Gogotsi Y, Trenary M, Tanaka T. Nanoindentation and Raman spectroscopy studies of boron carbide single crystals. Applied Physical Letters. 2002;81(20):3783-5.

22. Yan X, Tang Z, Zhang L, Guo J, Jin C, Zhang Y, et al. Depressurization amorphization of single-crystal boron carbide. Physical Review Letters. 2009;102(7):075505.

23. Yang Q, Hwang C, Marvel C, Chauhan A, Domnich V, Khan A, et al. Fabrication and characterization of arc melted Si/B co-doped boron carbide. Journal of the European Ceramic Society. 2019;39(16):5156-66.

24. Zhao S, Kad B, Remington B, LaSalvia J, Wehrenberg C, Behler K. Directional amorphization of boron carbide subjected to laser shock compression. Proceedings of the National Academy of Sciences of the United States of America. 2016;113(43):12088-93.

25. Chen M, McCauley J, Hemker K. Shock-induced localized amorphization in boron carbide. Science. 2003;299(5612):1563-6.

26. Rubink WS, Ageh V, Lide H, Ley NA, Young ML, Casem DT, et al. Spark plasma sintering of B_4C and B_4C-TiB_2 composites: Deformation and failure mechanisms under quasistatic and dynamic loading. Journal of the European Ceramic Society. 2021;41(6):3321-32.

27. Hwang C, DiPietro S, Xie KY, Yang Q, Celik AM, Khan AU, et al. Small amount TiB_2 addition into B_4C through sputter deposition and hot pressing. Journal of the American Ceramic Society. 2019;102(8):4421-6.

28. Yang Q, Çelik A, Du J, LaSalvia J, Hwang C, Haber R. Advancing the mechanical properties of Si/B co-doped boron carbide through TiB_2 reinforcement. Materials Letters. 2020;266:127480.

29. Xiang S, Ma L, Yang B, Dieudonne Y, Pharr G, Lu J. Tuning the deformation mechanisms of boron carbide via silicon doping. Science advances. 2019;5(10):eaay0352.

30. Chauhan A, Schaefer MC, Haber RA, Hemker KJ. Experimental observations of amorphization in stoichiometric and boron-rich boron carbide. Acta Materialia. 2019;181:207-15.

31. Schaefer MC, Haber RA. Amorphization Mitigation in Boron-Rich Boron Carbides Quantified by Raman Spectroscopy. Ceramics. 2020;3(3):297-305.

32. Holmquist TJ, Johnson GR. Characterization and evaluation of boron carbide for plate-impact conditions. Journal of Applied Physics. 2006;100(9):093525.

33. Grady DE. Shock-wave strength properties of boron carbide and silicon carbide. Le Journal de Physique IV. 1994;4(C8):C8-385-C8-91.

34. Chen M, McCauley JW. Mechanical scratching induced phase transitions and reactions of boron carbide. Journal of Applied Physics. 2006;100:123517.

35. Reddy K, Liu P, Hirata A, Fujita T, Chen M. Atomic structure of amorphous shear bands in boron carbide. Nature communications. 2013;4(1):2483.

36. Taylor DE. Shock compression of boron carbide: A quantum mechanical analysis. Journal of the American Ceramic Society. 2015;98(10):3308-18.

37. Aryal S, Rulis P, Ching W. Mechanism for amorphization of boron carbide (B_4C) under uniaxial compression. Physical review B. 2011;84:184112.

38. An Q, Goddard III WA, Cheng T. Atomistic explanation of shear-induced amorphous band formation in boron carbide. Physical Review Letters. 2014;113(9):095501.

39. An Q, Goddard III WA. Atomistic Origin of Brittle Failure of Boron Carbide from Large-Scale Reactive Dynamics Simulations: Suggestions toward Improved Ductility. Physical Review Letters. 2015;115(10):105501.

40. An Q, Goddard III WA. Microalloying Boron Carbide with Silicon to Achieve Dramatically Improved Ductility. The Journal of Physical Chemistry Letters. 2014;5(23):4169-74.

41. An Q, Goddard III WA. Ductility in crystalline boron subphosphide ($B_{12}P_2$) for large strain indentation. The journal of physical chemistry C. 2017;121(30):16644-9.

42. Lionel VG, F. SR, James C. Flexural Strength, Fracture Toughness, and Hardness of Silicon Carbide and Boron Carbide Armor Ceramics. International Journal of Applied Ceramic Technology. 2010;7(5):643-51.

43. Schwetz KA, Sigl LS, Pfau L. Mechanical Properties of Injection Molded B_4C–C Ceramics. Journal of Solid State Chemistry. 1997;133(1):68-76.

44. Telle R, Petzow G. Mechanisms in the liquid phase sintering of boron carbide with silicon based melts. High Tech Ceramics(Part A). 1987;38:961-73.

45. Dole SL, Prochazka S, Doremus RH. Microstructural Coarsening During Sintering of Boron Carbide. Journal of the American Ceramic Society. 1989;72(6):958-66.

46. Zhang W, Yamashita S, Kita H. Progress in pressureless sintering of boron carbide ceramics – a review. Advances in Applied Ceramics. 2019;118(4):222-39.

47. Jannotti P, Subhash G, Zheng JQ, Halls V, Karandikar PG, Salamone S, et al. Raman spectroscopic characterization of the core-rim structure in reaction bonded boron carbide ceramics. Applied Physics Letters. 2015;106(4).

48. Hayun S, Weizmann A, Dariel MP, Frage N. Microstructural evolution during the infiltration of boron carbide with molten silicon. Journal of the European Ceramic Society. 2010;30(4):1007-14.

49. Kolel-Veetil MK, Gamache RM, Bernstein N, Goswami R, Qadri SB, Fears KP, et al. Substitution of silicon within the rhombohedral boron carbide (B_4C) crystal lattice through high-energy ball-milling. Journal of Materials Chemistry C. 2015;3(44):11705-16.

50. Kieffer R, Gugel E, Leimer G, Ettmayer P. Investigations in the ternary system boron-carbon-silicon. Ber Deut Keram Ges. 1972;49(2):41-6.

51. Angers R, Beauvy M. Hot-pressing of boron carbide. Ceramics international. 1984;10(2):49-55.

52. Han W-Q. Silicon doped boron carbide nanorod growth via a solid-liquid-solid process. Applied Physics Letters. 2006;88(13):133118.

53. Khan AU, Etzold AM, Yang X, Domnich V, Xie KY, Hwang C, et al. Locating Si atoms in Si-doped boron carbide: A route to understand amorphization mitigation mechanism. Acta Materialia. 2018;157:106-13.

54. Ma L, Xie KY, Toksoy MF, Kuwelkar K, Haber RA, Hemker KJ. The effect of Si on the microstructure and mechanical properties of spark plasma sintered boron carbide. Materials Characterization. 2017;134:274-8.

55. Thévenot F. Boron carbide - A comprehensive review. Journal of the European Ceramic Society. 1990;6(4):205-25.

56. German RM, Suri P, Park SJ. Review: liquid phase sintering. Journal of Material Science. 2009;44:1-39.

57. Ghosh D, Subhash G, Zheng JQ, Halls V. Influence of stress state and strain rate on structural amorphization in boron carbide. Journal of Applied Physics 2012;111:063523.

58. DeVries M, Pittari III J, Subhash G, Mills K, Haines C, Zheng JQ. Rate-Dependent Mechanical Behavior and Amorphization of Ultrafine-Grained Boron Carbide. Journal of the American Ceramic Society. 2016;99(10):3398-405.

59. Moshtaghioun BM, Gomez-Garcia D, Dominguez-Rodriguez A, Todd RI. Grain size dependence of hardness and fracture toughness in pure near fully-dense boron carbide ceramics. Journal of the European Ceramic Society. 2016;36(7):1829-34.

60. Roy T, Subramanian C, Suri A. Pressureless sintering of boron carbide. Ceramics international. 2006;32(3):227-33.

61. Xie K, Domnich V, Farbaniec L, Chen B, Kuwelkar K, Ma L. Microstructural characterization of boron-rich boron carbide. Acta Materialia. 2017;136:202-14.

62. Jianxin D. Erosion wear of boron carbide ceramic nozzles by abrasive air-jets. Material Science and Engineering: A. 2005;408:227.

63. Sahin FC, Apak B, Akin I, Kanbur HE, Genckan DH, Turan A, et al. Spark plasma sintering of B_4C–SiC composites. Solid State Sciences. 2012;14(11):1660-3.

64. Uehara M, Shiraishi R, Nogami A, Enomoto N, Hojo J. SiC–B_4C composites for synergistic enhancement of thermoelectric property. Journal of the European Ceramic Society. 2004;24(2):409-12.

65. Zhang Z, Du X, Wang W, Fu Z, Wang H. Preparation of B_4C–SiC composite ceramics through hot pressing assisted by mechanical alloying. International journal of refractory metals and hard materials. 2013;41:270-5.

66. Uygun B, Göller G, Onüralp Y, Şahin FÇ, editors. Production and characterization of boron carbide–titanium diboride ceramics by spark plasma sintering method. Advances in Science and Technology; 2010: Trans Tech Publ.

67. Huang SG, Vanmeensel K, Malek OJA, Biest OVd, Vleugels J. Microstructure and mechanical properties of pulsed electric current sintered B_4C–TiB_2 composites. Materials Science and Engineering: A. 2011;528(3):1302-9.

68. Wenbo H, Jiaxing G, Jihong Z, Jiliang Y. Microstructure and properties of B_4C-ZrB_2 ceramic composites. International Journal of Engineering and Innovative Technology. 2013;3(1):163-6.

69. Zou J, Huang S-G, Vanmeensel K, Zhang G-J, Vleugels J, Biest OVd. Spark Plasma Sintering of Superhard B_4C–ZrB_2 Ceramics by Carbide Boronizing. Journal of the American Ceramic Society. 2013;96(4).

70. Hofmann H, Petzow G. Structure and properties of reaction hot-pressed B_4C-TiB_2-W_2B_5 materials. Journal of the Less Common Metals. 1986;117(1-2):121-7.

71. Sigl LS, Kleebe HJ. Microcracking in B_4C-TiB_2 composites. Journal of the American Ceramic Society 1995;78(9):2374-80.

72. Huang SG, Vanmeensel K, Biest OVd, Vleugels J. In situ synthesis and densification of submicrometer-grained B_4C-TiB_2 composites by pulsed electric current sintering. Journal of the European Ceramic Society 2011;31(4):637-44.

73. Celik AM. Investigation of the role of impurities and sintering parameters on the microstructure and properties of dense titanium diboride ceramics and boron carbide–titanium diboride composites: Rutgers University; 2020.

74. Munro RG. Material properties of titanium diboride. Journal of Research of the National Institute of Standards and Technology. 2000;105(5):709.

75. Wang Y-j, Peng H-x, Ye F, Zhou Y. Effect of TiB_2 content on microstructure and mechanical properties of in-situ fabricated TiB_2/B_4C composites. Transactions of Nonferrous Metals Society of China. 2011;21:s369-s73.

76. Skorokhod V, Krstic V. High strength-high toughness B_4C-TiB_2 composites. Journal of Materials Science Letters. 2000;19(3):237-9.

77. Tsagareishvili GV, Nakashidze, T. G. Jobava, J. Sh Lomidze, G. P. Khulelidze, D. E. Tsagareishvili, D. Sh Tsagareishvili, O. A. Thermal expansion of boron and boron carbide. Journal of the Less Common Metals. 1986;117(1-2):159-61.

78. Wei GC, Becher PF. Improvements in mechanical properties in SiC by the addition of TiC particles. Journal of the American Ceramic Society. 1984;67(8):571-4.

79. Niihara K, Nakahira A, Hirai T. The effect of stoichiometry on mechanical properties of boron carbide. Journal of the American Ceramic Society. 1984;67(1):C-13-C-4.

80. Cheng C, Reddy KM, Hirata A, Fujita T, Chen M. Structure and mechanical properties of boron-rich boron carbides. Journal of the European Ceramic Society. 2017;37(15):4514-23.

81. Savio SG, Ramanjaneyulu K, Madhu V, Bhat TB. An experimental study on ballistic performance of boron carbide tiles. International Journal of Impact Engineering. 2011;38(7):535-41.

82. King DS, Fahrenholtz WG, Hilmas GE. Silicon carbide–titanium diboride ceramic composites. Journal of the European Ceramic Society. 2013;33(15-16):2943-51.

83. Yamada S, Hirao K, Yamauchi Y, Kanzaki S. High strength B_4C–TiB_2 composites fabricated by reaction hot-pressing. Journal of the European Ceramic Society. 2003;23(7):1123-30.

84. Proctor JE, Bhakhri V, Hao R, Prior TJ, Scheler T, Gregoryanz E, et al. Stabilization of boron carbide via silicon doping. Journal of Physics: Condensed Matter. 2014;27(1):015401.

85. Khan AU, Domnich V, Haber RA. Boron carbide-based armors: problems and possible solutions. American Ceramic Society Bulletin. 2017;96(6):30-5.

86. Knight R, Smith RW, Apelian D. Application of plasma arc melting technology to processing of reactive metals. International Materials Reviews. 1991;36(1):221-52.

87. Sharma A, Kumar SA, Kushvaha V. Effect of aspect ratio on dynamic fracture toughness of particulate polymer composite using artificial neural network. Engineering Fracture Mechanics. 2020;228.

88. Li B, Xu L, Shi Y, Chi Y, Liu Q, Li C. Effects of fiber type, volume fraction and aspect ratio on the flexural and acoustic emission behaviors of steel fiber reinforced concrete. Construction and Building Materials. 2018;181:474-86.

89. Šajgalik P, Dusza J, Hoffmann MJ. Relationship between microstructure, toughening mechanisms, and fracture toughness of reinforced silicon nitride ceramics. Journal of the American Ceramic Society. 1995;78(10):2619-24.

90. Riedel R. Handbook of Ceramic Hard Materials: WILEY-VCH Verlag GmbH; 2000.

91. Guo D, Song S, Luo R, Goddard III WA, Chen M, Reddy KM, et al. Grain Boundary Sliding and Amorphization are Responsible for the Reverse Hall-Petch Relation in Superhard Nanocrystalline Boron Carbide. Physical Review Letters. 2018;121:145504.

92. Reddy KM, Guo JJ, Shinoda Y, Fujita T, Hirata A, Singh JP, et al. Enhanced mechanical properties of nanocrystalline boron carbide by nanoporosity and interface phases. Nature Communications. 2012;3:1052.

93. Tan Y, Zhang H, Peng S. Electrically conductive graphene nanoplatelet/boron carbide composites with high hardness and toughness Scripta Materialia. 2016;114:98-102.

94. Liu L, Wang Y, Li X, Xu L, Cao X, Wang Y, et al. Enhancing Toughness in Boron Carbide with Reduced Graphene Oxide. Journal of the American Ceramic Society. 2016;99(1):257-64.

Table 1. Physical and mechanical properties of the Si/B co-doped boron carbide and PAD B_4C. The flexural strength of PAD B_4C is taken from literature.(42)

Properties	Si/B co-doped	PAD B4C	%Δ

$Hv_{9.8N}$ (GPa)	25.0±0.9	26.6±0.5	-5
Indentation K_{1C}	2.06±0.2	2.25±0.14	-13
Young's modulus (E, GPa)	430±2	405	+6
Flexural strength (σ_f, MPa)	332±23	398±34*	-15
Density (g/cm^3)	2.49	2.50	~0
Average grain size (μm)	79.8±11.0	11.2±1.5	+654

Table 2. Properties of representative boron carbides reinforced with particulate SiC, TiB_2, and ZrB_2.(10, 42, 62-69) Fracture toughness were measured by either indentation(10, 62-64, 66, 67, 69), single-edge notched beam(65, 68), or chevron notch method(42).

System	Reinforce-ment amount	Processing method & condition	Density		Vickers hardness (GPa)	Fracture toughness ($MPa \cdot m^{1/2}$)	Ref.
			Real (g/cm^3)	Relative (%)			
B_4C	-	HP, 2150°C, 36 MPa, 60 min	2.41	95.5	32.5	2.5-3.0	(62)
	-	SPS, 1700°C, 75MPa, 3 min	2.50	99.4	39.3	3.5	(10)
	-	HP, Commercial plate	>2.50	> 99.0	25.8	2.7-2.9	(42)
B_4C-SiC	15 wt%	SPS, 1700°C, 75MPa, 3 min	2.59	99.4	36.2	5.7	(10)
	5 vol%	SPS, 1750°C, 40MPa, 5 min	2.50	98.0	34.4	-	(63)
	10 vol%	SPS, 1750°C, 40MPa, 5 min	2.54	98.0	33.4	-	(63)
	15 vol%	SPS, 1750°C, 40MPa, 5 min	2.57	97.8	31.1	-	(63)
	30 wt%	HP, 2000°C, 50MPa, 30 min	2.67	99.0	24.0	3.8	(64)

	50 wt%	HP, 1950°C, 30MPa, 30 min	2.71	96.0	24.0	4.6	(65)
B_4C-TiB_2	5 vol%	SPS, 1760°C, 40MPa, 60 min	2.57	98.1	34.5	5.0	(66)
	10 vol%	SPS, 1760°C, 40MPa, 60 min	2.67	98.3	32.5	6.9	(66)
	15 vol%	SPS, 1760°C, 40MPa, 60 min	2.79	99.2	32.0	6.0	(66)
	20 vol%	SPS, 1760°C, 40MPa, 60 min	2.89	99.2	32.5	5.3	(66)
	20 vol%	SPS, 2000°C, 60MPa, 6 min	2.92	99.9	32.5	3.2	(67)
	30 vol%	SPS, 2000°C, 60MPa, 6 min	3.12	100	31.2	-	(67)
	40 vol%	SPS, 2000°C, 60MPa, 6 min	3.32	100	30.5	4.4	(67)
	60 vol%	SPS, 2000°C, 60MPa, 6 min	3.72	100	29.0	4.5	(67)
	80 vol%	SPS, 2000°C, 60MPa, 6 min	4.09	99.3	26.3	4.8	(67)
B_4C-ZrB_2	20 vol%	HP, 2100°C, 30MPa, 60 min	3.08	95.2	30.4	6.3	(68)
	30 vol%	HP, 2100°C, 30MPa, 60 min	3.52	98.0	32.4	7.0	(68)
	40 vol%	HP, 2100°C, 30MPa, 60 min	3.86	97.8	28.8	6.6	(68)
	31 vol%	SPS, 1900°C, 60MPa, 5 min	3.61	100	31.1	3.0	(69)
	46 vol%	SPS, 2000°C, 60 MPa, 5 min	4.16	100	26.8	4.3	(69)

Table 3. Comparison of grain size and density between B_4C reinforced with 10% TiB_2 and monolithic B_4C.

Specimen	Average B_4C grain size (μm)	Average TiB_2 grain size (μm)	Bulk density, ρ (g/cm^3)	Relative density, ρ/ρ_{th} %
B_4C–10 wt% TiB_2	1.6 ± 0.5	1.25 ± 0.2	2.64	> 99.9
Monolithic B_4C	17.0 ± 2.1	–	2.52	> 99.9

Table 4. Mechanical properties of the commercial armor-grade boron carbide (PAD B_4C), monolithic B_4C and B_4C reinforced with TiB_2.

Properties	PAD B_4C	Monolithic B_4C	B_4C-10 %TiB_2
Vickers Hardness (GPa, @1kg)	26.6 ± 0.5	28.6 ± 1.1	32.9 ± 1.5
Indentation Toughness ($MPa.m^{1/2}$)	2.25 ± 0.14	2.29 ± 0.19	2.88 ± 0.21
Young's Modulus (GPa)	405	398	407
Density (g/cc)	2.50	2.48	2.60

Table 5. Physical and mechanical properties of Si-BC/TiB_2. Si-BC and commercial armor-grade B_4C (PAD B_4C) are listed for reference.

Specimen	TD (g/cc)	$H_{V, 9.8N}$ (GPa)	Indentation K_{1C} ($MPa \cdot m^{0.5}$)	Strength (MPa)	E (GPa)	Amorphization reduction
Si-BC/TiB_2	2.62	26.6 ± 0.9	2.3 ± 0.2	410 ± 52	427	-39.2 ± 4.6 %
Si-BC	2.50	25.0 ± 0.9	2.1 ± 0.2	338 ± 30	430	-36.9 ± 10.5%
Commercial	2.49	26.5 ± 0.5	2.4 ± 0.1	398 ± 34	406	Reference

List of Table and Figure Captions

[Table Captions]

Table 1. Physical and mechanical properties of the Si/B co-doped boron carbide and PAD B_4C. The flexural strength of PAD B_4C is taken from literature.(42)

Table 2. Properties of representative boron carbides reinforced with particulate SiC, TiB_2, and ZrB_2.(10, 42, 62-69) Fracture toughness were measured by either indentation(10, 62-64, 66, 67, 69), single-edge notched beam(65, 68), or chevron notch method(42).

Table 3. Comparison of grain size and density between B_4C reinforced with 10% TiB_2 and monolithic B_4C.

Table 4. Mechanical properties of the commercial armor-grade boron carbide (PAD B_4C), monolithic B_4C and B_4C reinforced with TiB_2.

Table 5. Physical and mechanical properties of Si-BC/TiB_2. Si-BC and commercial armor-grade B_4C (PAD B_4C) are listed for reference.

[Figure Captions]

Fig. 1. Hardness and density of representative structural and hard materials.(5-10)

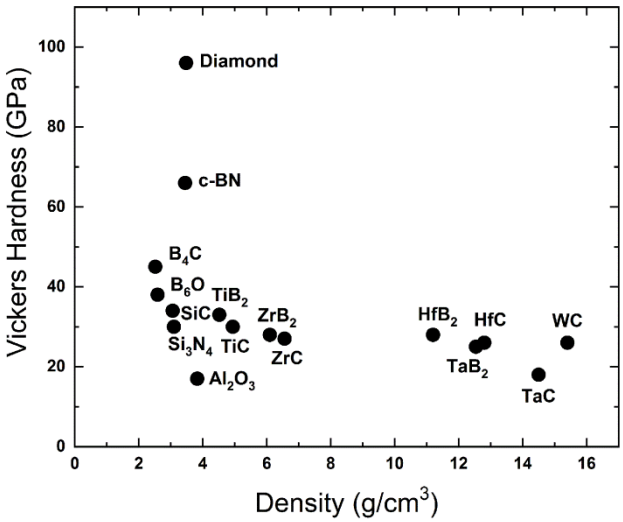

Fig. 2. The crystal structure of boron carbide.(11, 12)

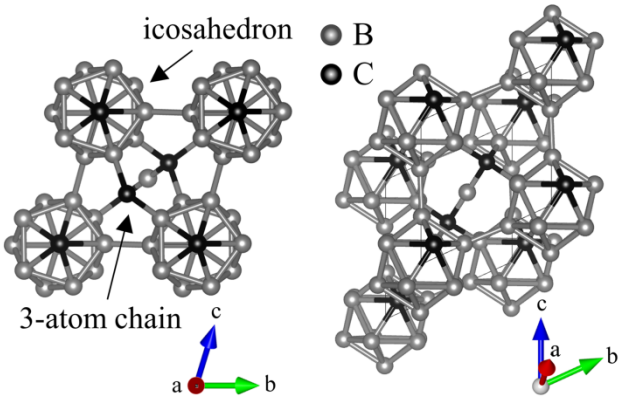

Fig. 3. The two major failure modes of boron carbide. (A) Boron carbide fails through a transgranular fracture mode: the fracture surface of boron carbide after a three-point flexural test.(26) (B) High-pressure loading triggers amorphization in boron carbide: an amorphous band observed in a fragment after a ballistic test; the insets show FFT (Fast Fourier transform) patterns confirming the amorphous nature of region (a) surrounded by the crystalline region (b).(25) Reproduced from Rubink et al.(26) and Chen et al.(25) with permission.

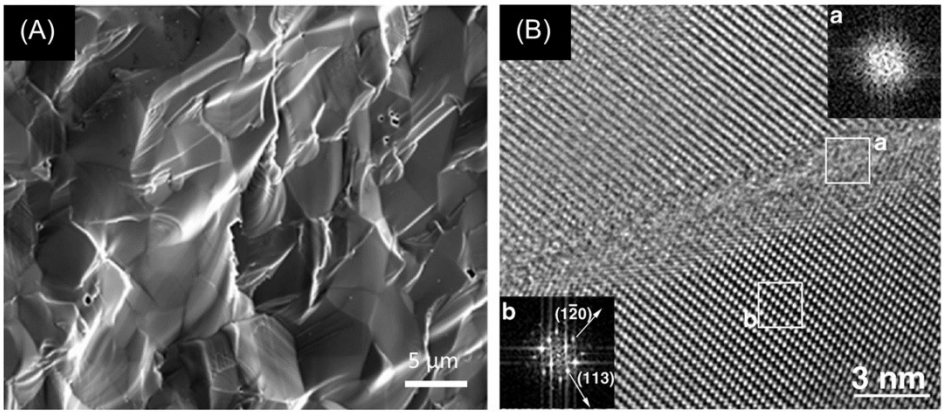

Fig. 4. Raman spectra of boron carbide ($B_{4.3}C$) before (a) and after (b) 100 mN indentation at several laser wavelengths (514.5 nm, 630 nm, and 780 nm). Arrows indicate (a) 1570 cm^{-1} peak of the pristine surface and (b) the new peaks appearing after indentation. Reproduced from Domnich et al.(21) with permission.

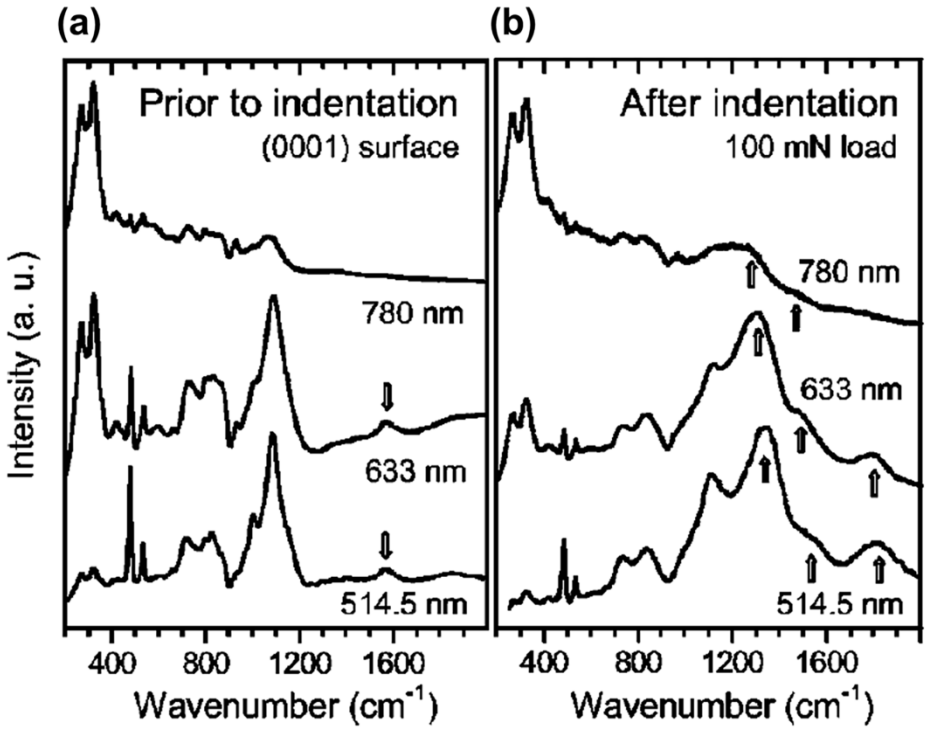

Fig. 5. The high-resolution STEM image showing the amorphous structure of the shear band along the $(01\bar{1}\bar{1})$ plane. Inset FFT patterns demonstrate the amorphous nature of the shear band. Reproduced from Reddy et al.(35) with permission.

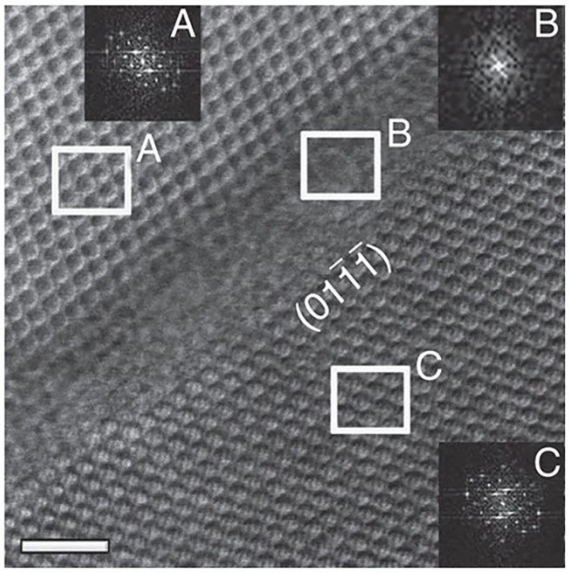

Fig. 6. The structures evolution of B_4C under shear along $(01\bar{1}\bar{1})/[\bar{1}101]$ slip system: (a) The structure at 0.209 strain with no bond breaking. (b) At 0.245 strain, the B-C bond connecting two icosahedra breaks, leading to the formation of carbene (marked with a circle). (c) The C-B-C chain approach the carbene at 0.331 strain. (d) The carbene reacts with the B atom in the C-B-C chain (red circle), deconstructing the cage (black circle). Reproduced from An et al.(38) with permission.

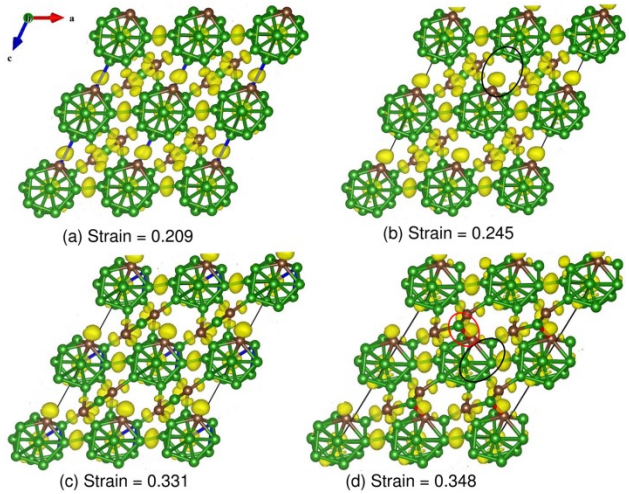

Fig. 7. (a) The $(B_{11}C_p)Si_2$ structure transition under shear along $(01\bar{1}\bar{1})/[\bar{1}101]$ slip system: (a) the intact structure; (b) the structure corresponds to the maximum stress; (c) the structure where the B−C bonds between icosahedra break; (d) the structure where the Si−Si bonds in the chain break and the Si atoms rebond to the unbonded B, C atoms from previous breaking B−C bond,; and (e) the transformed structure with new formed Si−Si bond and B−B bond between icosahedra. Reproduced from An et al.(40) with permission.

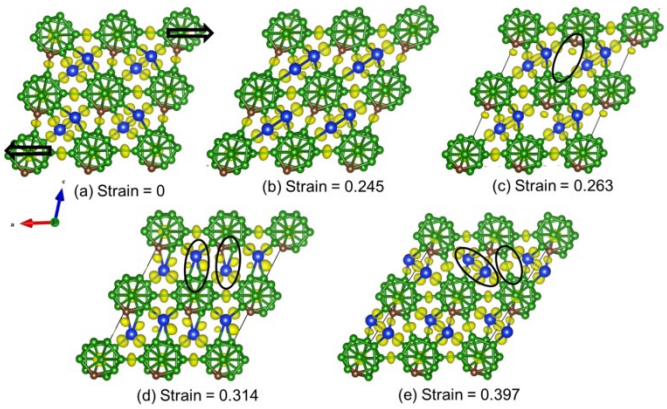

Fig. 8. (a) XRD patterns, (b) Raman spectra, and (c) SEM images of Si/B co-doped boron carbide and commercial PAD B_4C. The enlarged section in the XRD shows a downward shift in the (021) peak, indicating a larger unit cell in the Si/B co-doped boron carbide than that of the PAD B_4C. Reproduced from Yang et al.(28) with permission.

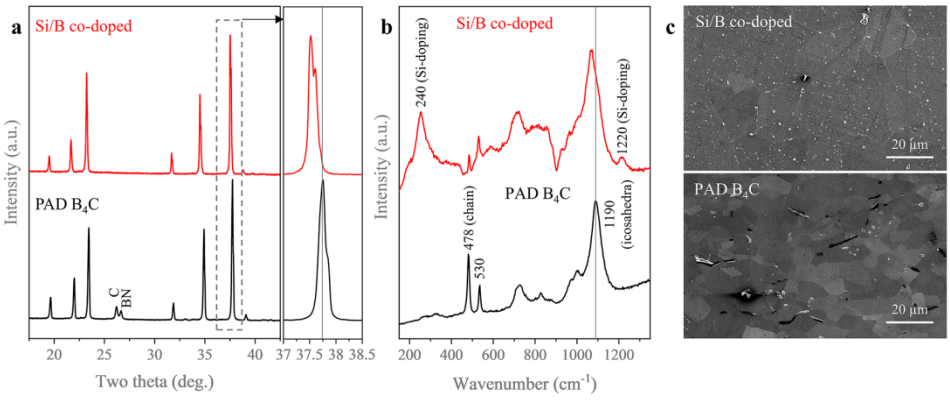

Fig. 9. (a) Amorphization intensity color map of PAD B_4C vs Si/B co-doped boron carbide. A reduction of 34% in amorphization area and 44% in amorphization intensity from the PAD B_4C to Si/B co-doped were obtained. Results from 5 individual 4.9N Vickers indents were averaged to construct the color map. Each image is 20 x 20 μm. (b) Amorphization pixel population histogram illustrating that Si/B co-doping is effective at suppressing the most intense amorphization.

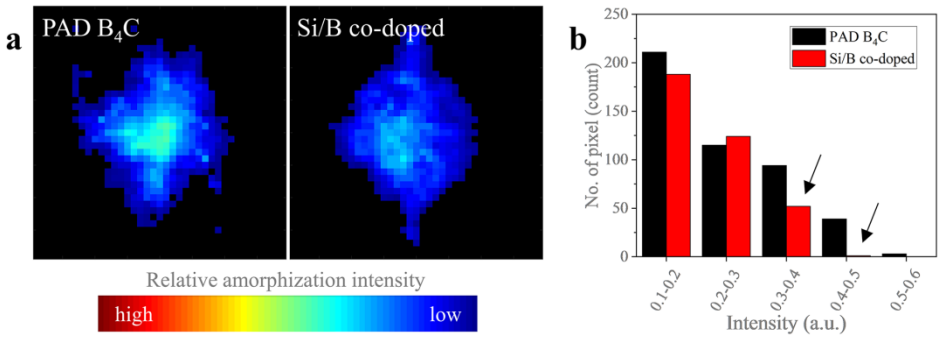

Fig. 10. SEM micrographs of B_4C fragments produced after an impact test showing cleavage surface at (a) low and (b) high magnification. (c) a TEM micrograph showing that most of the boron carbide grains had clean grain boundary (no or few defects or intergranular films). (d) a SEM micrograph showing a fracture surface of hot pressed boron carbide. Reproduced from Chen et al., Xie et al., Roy et al. with permission.(20, 25, 60)

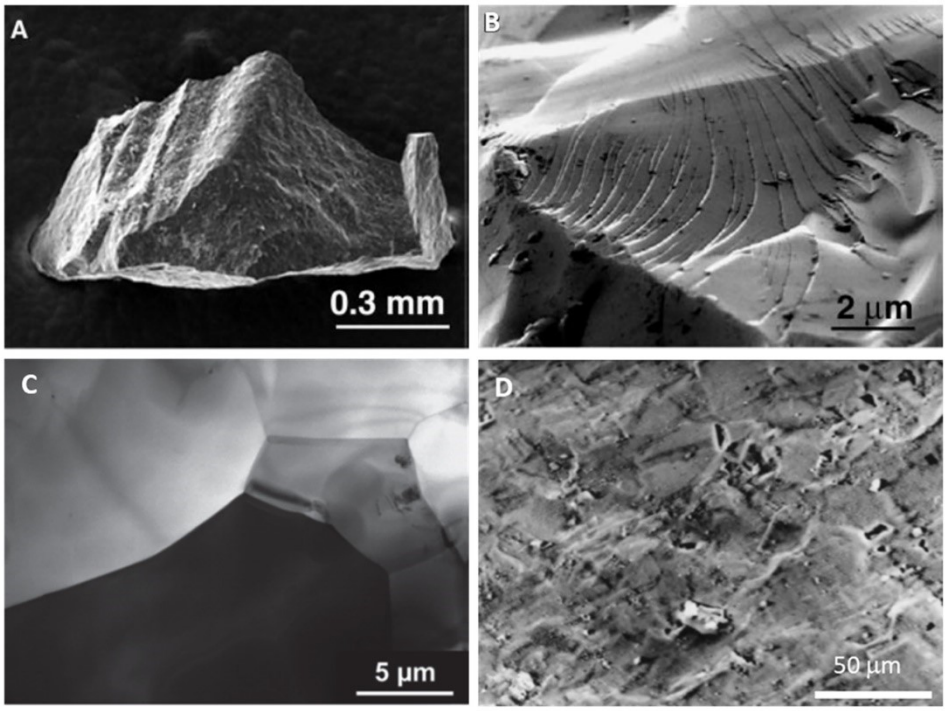

Fig. 11. Changes in (a) toughness and (b) hardness of B_4C composites by adding reinforcements of SiC, TiB_2, and ZrB_2.(10, 42, 62-69)

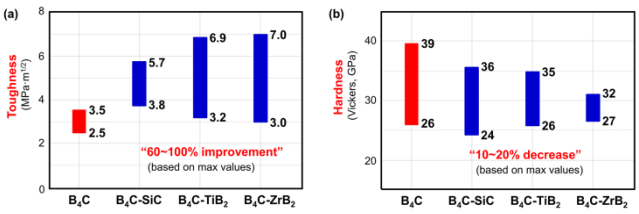

Fig. 12. X-ray diffraction pattern of B_4C-10 wt.% TiB_2 composite along with those of starting B_4C and TiB_2 powders.

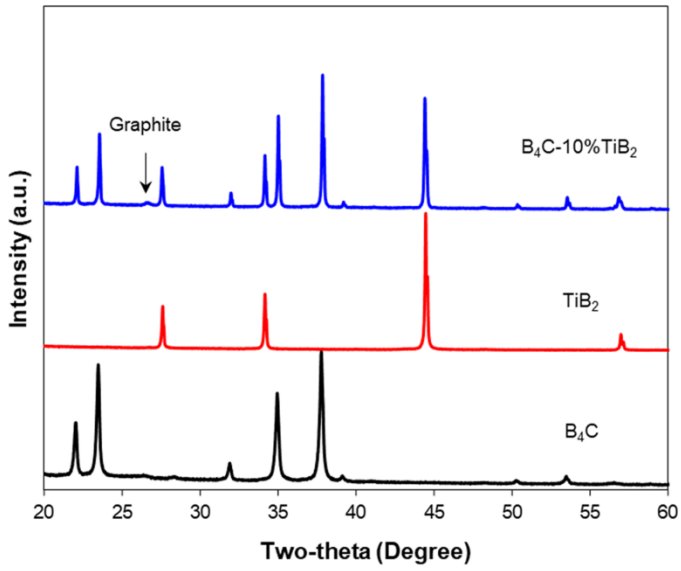

Fig. 13. Microstructural observation of B_4C-10% TiB_2 at (a) low and (b) high magnifications. (c) grain boundaries of the B_4C matrix were highlighted under the InLens detector: TiB_2 is the dark phase, and (d) monolithic B_4C sample prepared at the same conditions is also prepared for comparison.

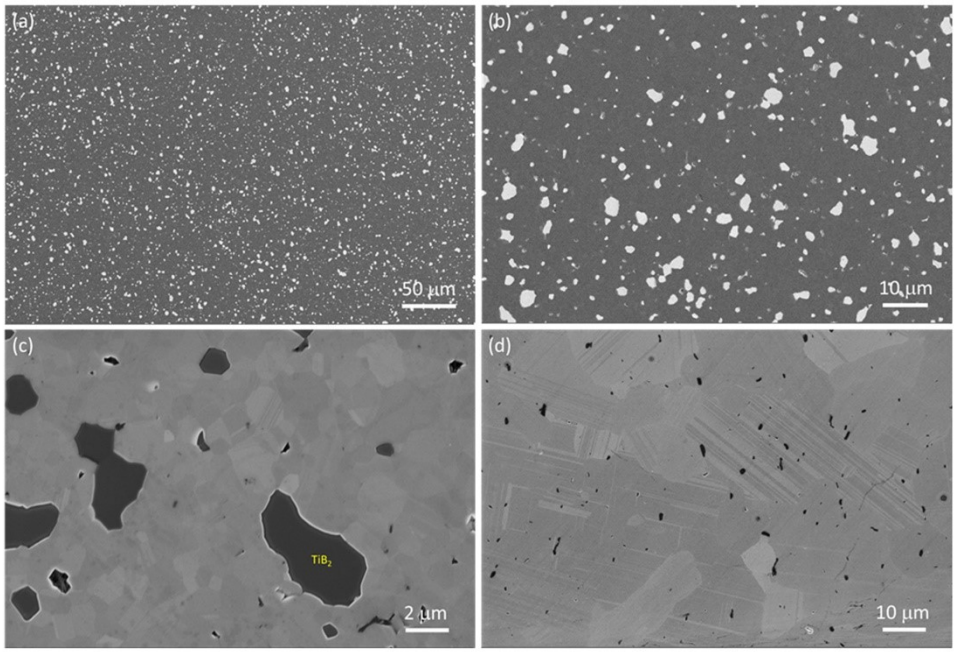

Fig. 14. (a) An optical micrograph of a Vickers' indent on TiB_2 reinforce B_4C (15 wt% TiB_2), showing cracks emanating from four corners. (b) A SEM micrograph showing a closer observation of the crack tip, showing a mixed fracture mode: transgranular (within B_4C matrix) and intergranular (at the interface between B_4C and TiB_2).

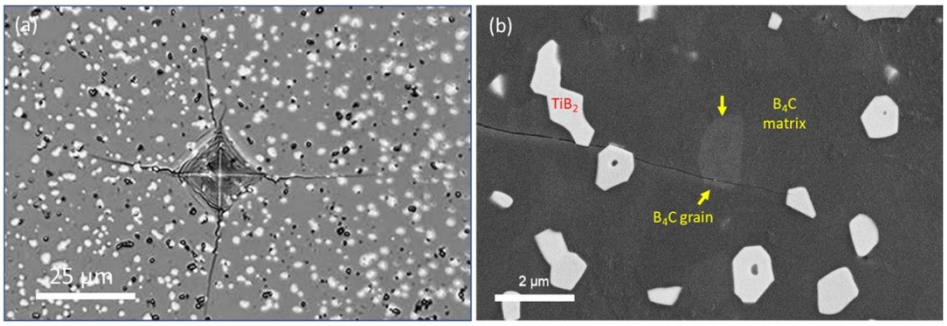

Fig. 15. SEM micrographs of polished Si-BC/TiB_2. (a) A dense microstructure with TiB_2 particles (bright phase) uniformly distributed throughout the material. (b) The minor secondary phase was identified in the Si-BC matrix. (c) Fine grain in the Si-BC matrix measured to be 1.5 µm on average.

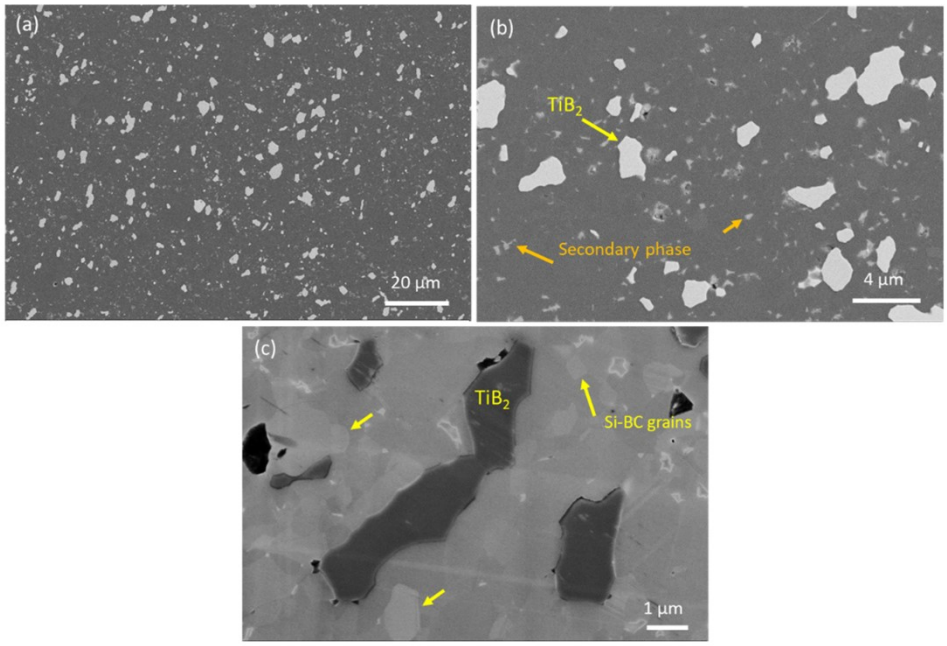

Fig. 16. (a) X-ray diffraction pattern and (b) Raman spectrum of Si-BC/TiB_2, where B_4C/TiB_2 was also included as a reference.

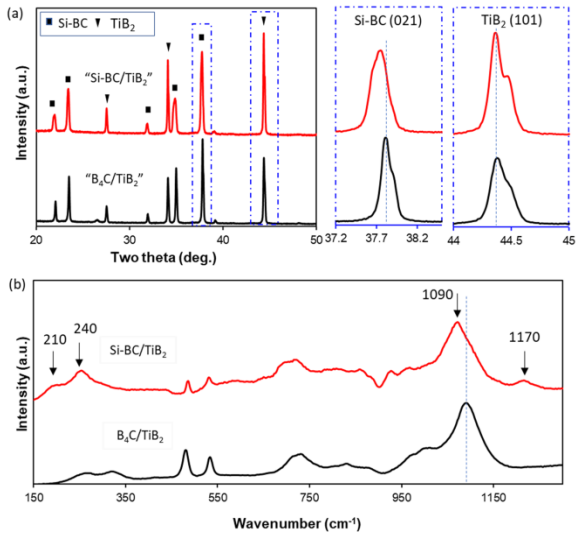

Fig. 17. Amorphization intensity pseudo-color map of Si-BC/TiB_2 vs. B_4C/TiB_2.

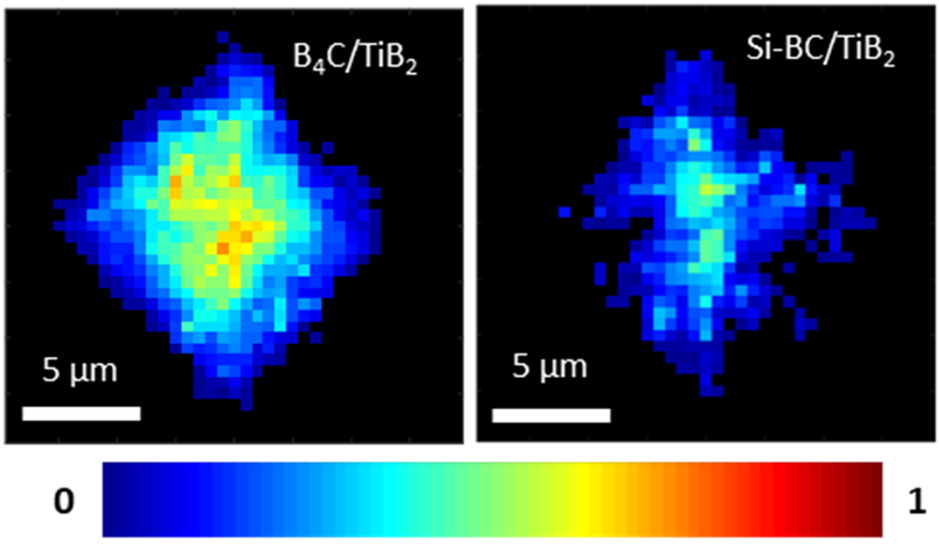

Fig. 18. Crack propagation behavior in (a) Si-BC/TiB_2 and (b) Si-BC matrix. Intergranular fracture was evidenced by crack deflection at the interface between Si-BC matrix and TiB_2 particles. On the other hand, the Si-BC experienced a transgranular fracture through multi-grains (as marked by arrows).